NANOINDENTATION OF ZnSnO/Si THIN FILMS PREPARED BY AEROSOL SPRAY PYROLYSIS

V. MORARI[1], C. PYRTSAC[2], N. CURMEI[2], D. GRABCO[2], E.V. RUSU[1],
V. V. URSACHI[3], I. M. TIGINYANU[3]

[1] *D. Ghitu* Institute of Electronic Engineering and Nanotechnology, MD-2028 Chisinau,
Republic of Moldova
[2] Institute of Applied Physics, MD-2028 Chisinau, Republic of Moldova
[3] National Center for Materials Study and Testing, Technical University of Moldova,
MD-2004 Chisinau, Republic of Moldova
E-mail: vvursaki@gmail.com

Abstract. Thin ZnSnO films with different thickness deposited on Si substrates by aerosol spray pyrolysis were investigated by *scanning electron microscopy* (SEM), *energy dispersive X-ray analysis* (EDX), *X-ray diffraction* (XRD), *atomic force microscopy* (AFM) and *light microscopy* (LM) using depth-sensitive nanoindentation with Berkovich indenter. The values of the Young modulus (E), nanohardness (H), and plasticity index (H/E) of the prepared films were determined according to the Oliver-Pharr method in the diapason of the applied loads of 30–300 mN. The main factors contributing to the nanomechanical properties of film-substrate structures were identified, and the deformation mechanisms of the ZnSnO/Si *coated system* (CS) under nanoindentation have been revealed.

Key words: Thin metal oxide semiconductor films, aerosol spray pyrolysis, nanoindentation, deformation mechanisms.

1. INTRODUCTION

Metal semiconductor oxides are prospective materials for a wide range of applications, including gas, chemical and biological sensors, supercapacitors, solar cells, fuel cells and batteries, pyroelectric, catalysts, anticorrosion coatings, etc. [1, 2]. Among them, binary ZnO and SnO_2 oxides have high potential for applications as phosphors, transparent conducting films, field emission devices, varistors, piezoelectric transducers, resonators, and sensors [3–8].

Zinc stannate (ZTO) has been considered as alternative to the binary oxides (ITO, SnO_2, ZnO) for potential applications in optoelectronic devices and solar energetics, due to its low cost, high optical transparency and low electrical resistivity, high electron mobility, and good stability [9]. Solid solutions can be formed in the ZnSnO system in an amorphous phase. As concerns the crystalline material, cubic perovskite or $LiNbO_3$ (LN) type $ZnSnO_3$, and cubic inverse spinel Zn_2SnO_4 crystals are formed in this system [9, 10]. ZTO materials have been prepared by a variety

of technological methods such as chemical vapor deposition (CVD), reactions under pressure, hydrothermal synthesis, sol-gel methods etc. [10].

ZTO thin films have been deposited on various substrates by *pulsed laser deposition* (PLD) [11], *thermal atomic layer deposition* (TALD) [12], hydrothermal method [13], magnetron sputtering [14, 15], and spray pyrolysis [16–18]. Among these methods, the spray pyrolysis was shown to be attractive due to its safety, suitability for production of high quality large-area films, and cost efficiency ensured by simplicity and non-vacuum system of deposition [18].

In spite of the fact that nanomechanical properties, such as hardness, plasticity, and fragility have a strong impact upon the quality and reliability of devices and are very important for many applications, they have been less investigated in the ZnSnO/Si *coated system* (CS) as compared to other properties. The goal of this paper was to investigate peculiarities of deformation under indentation, to determine the main mechanical parameters such as Young modulus (E) and nanohardness (H) of ZnSnO films and ZnSnO/Si CSs, and the plasticity index of (H/E) the prepared composites, and to evaluate their modification as a function of the film thickness and the value of the load applied to the indenter.

2. SAMPLE PREPARATION AND EXPERIMENTAL DETAILS

ZnSnO films were deposited by aerosol spray pyrolysis method. A solution of 0.5 M zinc nitrate [$Zn(NO_3)_2$] and 0.5 M tin chloride [$SnCl_4$] dissolved in ethanol [C_2H_5OH], was sprayed onto the Si(111) substrate using a sprayer with an O_2 gas flow from an oxygen gas cylinder with the outlet pressure of 1.1 atmospheres. The zinc nitrate and tin chloride solutions with respective ratio were mixed in an ultrasonic bath during 15 minutes at a temperature of 50–60°C before the deposition process. The substrate was heated in the temperature range of 420°C to 480°C during the deposition. The produced film thickness is determined by the rate of precursor solution injection and the duration of deposition process. Usually, an injection rate of 1 ml/min was used, and the deposition process last from 15 minutes to one hour.

The morphology and chemical composition microanalysis of the produced films were studied using a TESCAN TS 5130MM scanning electron microscope equipped with tools for *energy dispersive X-ray* analysis (EDX). *Atomic force microscopy* (AFM) measurements were performed with Nanostation instrument. *X-ray diffraction* (XRD) measurements were carried out on a Rigaku SmartLab X Ray Diffractometer using CuK$_\alpha$ radiation ($\lambda = 0.15406$ nm). Microstructural studies were carried out using the Amplival and XJL-101 light microscopies (LM) with digital monitoring and the Linnik MII-4 microinterferometer.

The mechanical properties of ZnSnO films with different thicknesses deposited onto Si(111) substrates were investigated by depth-sensitive nanoindentation with a Nanotester-PMT3-NI-02 instrument equipped with a Berkovich indenter. The testing

was performed for 4 values the maximum load applied to the indenter (P_{max} = 30, 50, 100 and 300 mN), according to the following scheme: (i) loading (penetration) stage up to the load maximum value ($P_{\max}$) during 20 s; (ii) maintaining the maximum load value on the indenter during 5 s; (iii) unloading (removal of the load) during 20 s. Up to five imprints were generated for each $P_{\max}$ value. The values of the Young modulus (E) and the hardness (H) of the investigated structures were deduced for each imprint from the dependence of the indenter penetration depth (h) upon the value of the applied load $P_{\max}$, according to the Oliver-Pharr method [19, 20]. The nanohardness was calculated according to the following equation:

$$H = \frac{P_{\max}}{A} \tag{1}$$

where $P_{\max}$ is the maximum value of the load on the indenter, and A is the imprint area.

The Young modulus was calculated according to the following equations:

$$\frac{1}{E_r} = \frac{(1-\nu^2)}{E} + \frac{(1-\nu_i^2)}{E_i} \tag{2}$$

where E_r is the reduced elasticity modulus, calculated according to the Eq. 3, E and ν are the elasticity modulus and the Poisson coefficient of the sample, E_i and ν_i are the elasticity modulus and the Poisson coefficient of the indenter.

$$E_r = \frac{\sqrt{\pi} \cdot S}{2\beta \cdot \sqrt{A_p(h_c)}} \tag{3}$$

The presented data are arithmetic mean of values measured for each imprint. All calculations are performed with the computer software program.

3. MORPHOLOGY COMPOSITION AND CRYSTAL STRUCTURE CHARACTERIZATION OF THE PREPARED FILMS

ZnSnO films with various thicknesses were obtained by varying the duration of the deposition process, as described in the experimental section. Figure 1 illustrates SEM images of three films with mean thicknesses of 445 nm, 670 nm, and 1410 nm.

The roughness parameters of films were determined from the analysis of AFM images presented in Fig. 2. The AFM images suggest that the films are

composed of crystallites with the size from 300 nm to 2 μm, while the roughness determined with the Gwyddion program was of R_a = 6.5 nm, 8.5 nm and 9.2 nm for the ZnSnO thin films with thickness t = 445 nm, 670 nm, and 1410 nm, respectively.
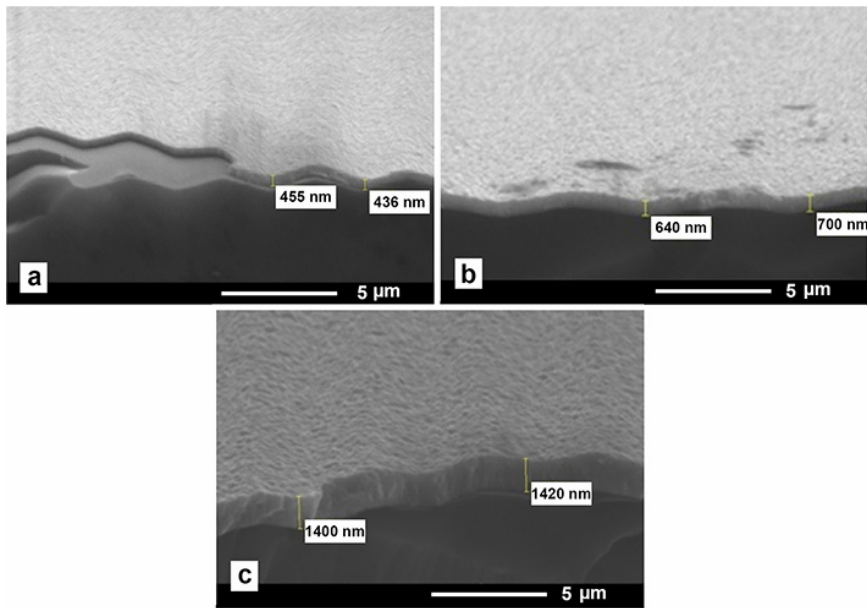

Fig. 1 – SEM images of ZnSnO thin films with mean thickness of 445 nm (a), 670 nm (b), and 1410 nm (c), obtained with different duration of the deposition process.
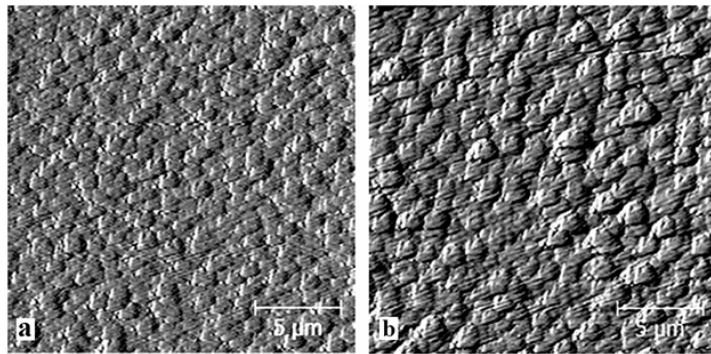

Fig. 2 – AFM images of ZnO layers prepared by aerosol spray pyrolysis (a) and Er-doped ZnO layers deposited by magnetron sputtering (b).

The elemental composition of these films determined from EDX analysis is presented in Table 1. The EDX analysis shows that the produced films are composed mainly of SnO_2 crystallites with some inclusion of a ZTO component.

Table 1

Elemental composition of ZnSnO films with different thicknesses

445 nm film			670 nm film			1410 nm film		
Element	Weight %	Atomic %	Element	Weight %	Atomic %	Element	Weight %	Atomic %
O	23.79	65.31	O	25.54	61.12	O	27.83	57.24
Zn	3.86	2.68	Zn	5.29	4.73	Zn	8.12	6.35
Sn	72.35	32.01	Sn	69.17	34.15	Sn	64.05	36.41
Total	100	100	Total	100	100	Total	100	100

The XRD pattern (Fig. 3) corroborates the results of the EDX analysis, confirming a two-phase composition of ZnSnO films, with the cassiterite SnO_2 (JCPDS 14-1445) and Zn_2SnO_4 zinc stannate as a second phase [21, 22].
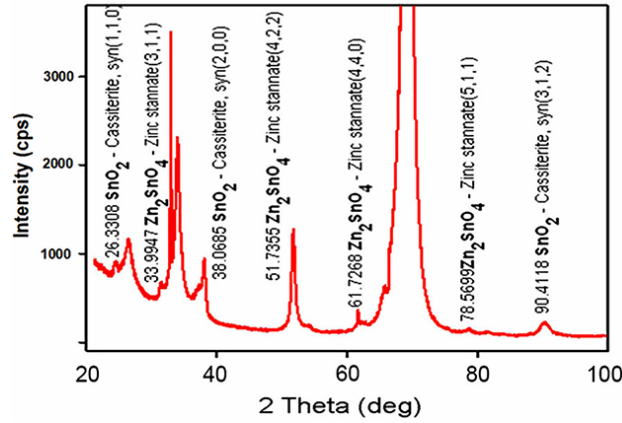

Fig. 3 – XRD pattern of a ZnSnO film deposited by aerosol spray pyrolysis on a Si substrate.

One can deduce from the analysis of data in Table 1, that the content of the Zn_2SnO_4 component in ZnSnO films increases with increasing the film thickness, the ration of Zn_2SnO_4:SnO_2 formula units being 1:23 for the 445 nm film, 1:13.5 for the 670 nm film, and 1:10.4 for the 1410 nm film.

The mean sizes of the Zn_2SnO_4 crystallites deduced from the analysis of the (4,2,2) reflex at 61.7°, according to the Scherrer formula (Eq. 4) [23], is 22 nm.

$$\tau = \frac{0.9\lambda}{\beta \cos\Theta} \qquad (4)$$

where τ is the mean size of the crystalline domains, λ is the X-ray wavelength, β is the line broadening at half the maximum intensity (FWHM) in radians, and Θ is the Bragg angle.

Therefore, one can conclude that smaller Zn_2SnO_4 nanocrystals with the mean size of 22 nm are dispersed between larger SnO_2 micro-crystallites.

4. INVESTIGATION OF NANOMECHANICAL PARAMETERS

Figure 4 presents the dependences of hardness H and Young modulus E upon the value of the load applied to the indenter. An insignificant dependence of these parameters upon the value of the load is observed for the single crystal Si substrate (curve 1), while the dependences for ZnSnO films deposited on Si substrates are much stronger. For instance, the films with the thickness $t_2 = 670$ nm and $t_3 = 1410$ nm show an increase of the hardness $\Delta H_i = (H_i - H_{Si}) / H_{Si} \cdot 100\%$ by 18.8% and 32.9%, respectively, as compared to the Si substrate at $P_{max} = 50$ mN (Table 2). The curves 3 and 4 for these films are situated above the curve for the Si substrate at low loads ($P \leq 100$ mN), while they are below that curve for high loads ($P > 100$ mN). At the same time, the hardness of the film with thickness of 445 nm is lower than the hardness of the Si substrate for all the applied loads.
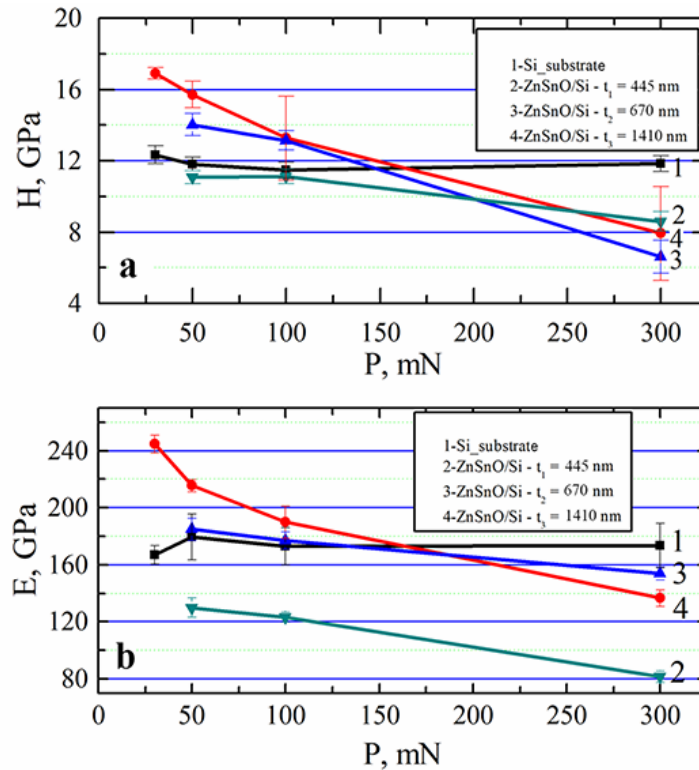

Fig. 4 – H(P) (a) and E(P) (b) dependencies for Si substrate (curve 1) and for ZnSnO/Si CSs (curves 2, 3, 4).

The values of ΔH_{445}, ΔH_{670} and ΔH_{1410} for $P_{max} = 300$ mN are equal to –27.4%, –44.1% and –33.2%, respectively, *i.e.* the hardness of the film-substrate structures decreased by around one third as compared to the hardness of the substrate (Table 2). The hardness of a film-substrate structure with a pure SnO_2 film with thickness similar to the first ZnSnO film and nearly the same roughness is also lower than the hardness of the Si substrate, according to previous investigations [24]. However, the hardness was nearly constant with increasing the load from 100 mN to 300 mN, similarly to the dependence observed for the single crystal Si substrate.

Table 2

Modification of hardness (ΔH) and Young's modulus (ΔE) values of ZnSnO/Si CSs with different ZnSnO film thicknesses (t_1, t_2, t_3) for different P_{max} loads applied to the indenter

P_{max}, mN	$\Delta H = (H_i - H_{Si}) / H_{Si} \cdot 100\%$			$\Delta E = (E_i - E_{Si}) / E_{Si} \cdot 100\%$		
	ΔH_{445}	ΔH_{670}	ΔH_{1410}	ΔE_{445}	ΔE_{670}	ΔE_{1410}
30	–	–	37	–	–	46.5
50	–6.35	18.8	32.9	–27	2.9	19.8
100	–0.27	12.0	13.2	–29	2.4	9.8
300	–27.4	–44.1	–33.2	–53	–10.7	–20.8

A similar dependence is observed for the Young modulus $E(P)$ (Fig. 4b) in all the diapason of loads $P_{max} = (30 \div 300)$ mN. The film with thickness $t_3 = 1410$ nm shows an increase of the Young modulus by 19.8% as compared to the Si substrate at $P_{max} = 50$ mN, while the film with thickness $t_1 = 445$ nm demonstrates a decrease by 27%. The largest decrease of the Young modulus is observed for the film with smallest thickness $t_1 = 445$ nm at $P_{max} = 300$ mN. This film demonstrates lower values of the Young modulus in all the diapason of loads as compared to the Si substrate as well as to the structures with thicker films, indicating therefore on the importance of the film thickness. However, the composition is also important, since the Young modulus of the structure with a pure SnO_2 film shown an increase of the Young modulus from 160 GPa to 180 GPa with increasing the load from 100 mN to 300 mN [24], in contrast to the decrease of the Young modulus with increasing the load observed in structures with the composite films. This effect is even more evident when assessing the plasticity index H/E. This parameter describes the wear resistance of materials, *i.e.*, the higher is the value of the H/E parameter the higher is the wear resistance [25, 26].

Figure 5 reflects the variations of the plasticity index $(H/E)_1$, $(H/E)_2$, $(H/E)_3$ of the investigated structures. The analysis of the H/E(P) dependences shows that the curve for the film with thickness $t_1 = 445$ nm exhibits at ascending trend (curve 2 in Fig. 5).

The plasticity index for this structure is much higher that its value for the Si substrate for all the applied loads, and it reaches a value of 0.106 at $P_{max} = 300$ mN,

which is 1.56 times higher than the $(H/E)_{Si}$ value of the substrate. It means that the ZnSnO film with this thickness improves the wear resistance when deposited on the Si substrate. In contrast to this, the $(H/E)_2$ and $(H/E)_3$ dependences (curves 3 and 4) show a descending behavior for structures with the ZnSnO films thickness of $t_2 = 670$ nm and $t_3 = 1410$ nm, so that the value of the plasticity index for such structures at $P_{max} = 300$ mN is much lower than its value $(H/E)_{Si}$ for the substrate. It means that the wear resistance of ZnSnO/Si coated structures decreases at the penetration of the indenter with increasing the film thickness.
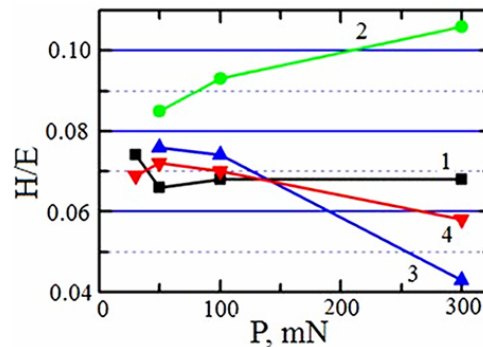

Fig. 5 – Dependencies that reflect variations in the H/E plasticity index with changing the P_{max} load value for ZnSnO/Si CSs with different film thicknesses. Curve 1 is for the Si sample, while curves 2, 3, 4 are for CSs samples with film thickness of t_1, t_2 and t_3, respectively.

One can explain the observed peculiarities of H(P), E(P) and H/E(P) curves on the basis of a detailed investigation of the imprint microstructure and the surface relief around the imprints as well as on the basis of the analysis of the "load – indenter penetration depth" $P(h)$ dependences for the investigated structures.

Images of the Berkovich imprints are presented in Fig. 6. Light microscopy was employed to reveal the relief in the region of imprints on the surface of ZnSnO/Si structures (Fig. 6 a-i), as well as on surface of the Si substrate (Fig. 6 j-l). The surface microstructure in the imprint region on the Si substrate is very smooth (Fig. 6 j, k, l). The imprints exhibit a plastic character, without damage, for load values of $P_{max} = 50$ and 100 mN. Very fine micro-cracks appear sometimes at the tip of imprints for the load of $P_{max} = 300$ mN only. The analysis of plastic deformation peculiarities of ZnSnO/Si structures (Fig. 6 a-i) demonstrates a more pronounced fragility of the film as compared to the fragility of the Si single crystal. Small cracks are observed starting with a load of $P_{max} = 50$ mN, and the length of these cracks gradually increases with increasing the load, while the area in the region of the imprint is sometimes accompanied by a cleavage of the material (Fig. 6 c, f). This fact leads to the decrease of the hardness H and the Young modulus E of the ZnSnO/Si CSs practically for all the values of the applied load P_{max}, exhibiting a descendent character of the $H(P)$ and $E(P)$ curves (see Fig. 4).
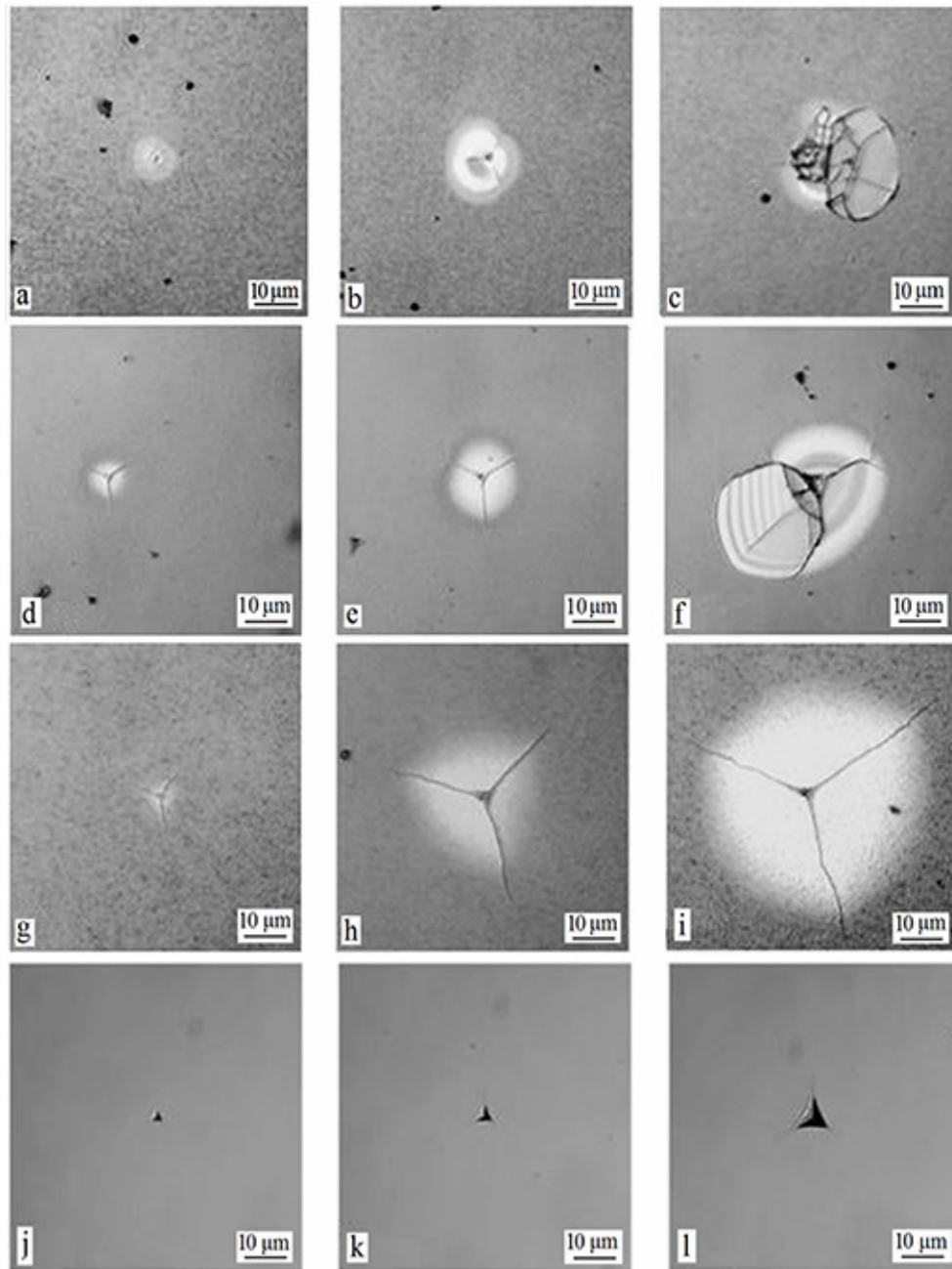
Fig. 6 – LM images of Berkovich imprints for different P_{max} loads applied to the ZnSnO/Si CSs as follows: a, d, g, j for 50 mN; b, e, h, k for 100 mN; c, f, i, l for 300 mN. Images a, b, c are for the film thickness t_1 of 445 nm; d, e, f are for t_2 of 670 nm; g, h, i are for t_3 of 1410 nm; j, k, l are for the Si substrate.

The images registered in the interference mode reveal that the area around the imprints, which contains cracks, is brighter than the other surface of the ZnSnO/Si samples (Fig. 7). This effect indicates on the fact that the bright area around the imprints is due to internal stresses of the structure inside the film, and due to some structural modifications. Some exfoliations of the film from the substrate are not excluded.
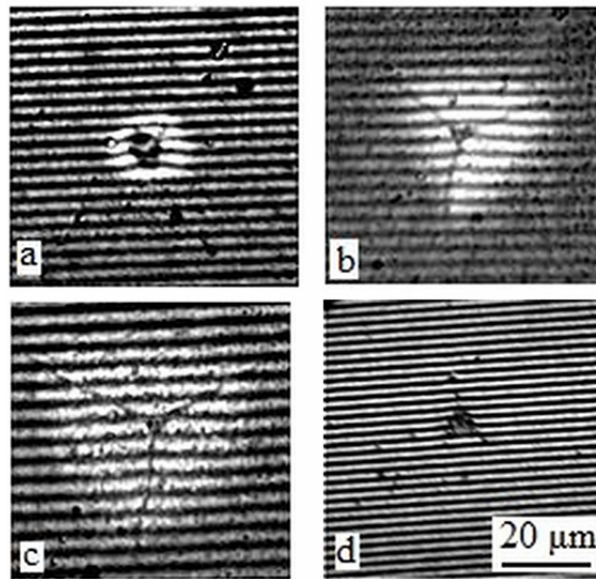

Fig. 7 – LM images of areas around the imprints measured in the interference mode for ZnSnO/Si CSs (a-c) and Si single crystal (d). Image (a) is for the film thickness $t_1 = 445$ nm; (b) is for $t_2 = 670$ nm; (c) is for $t_3 = 1410$ nm. The applied load P is 50 mN in (a); 100 mN in (b); and 300 mN in (c,d). The scale is the same for all images.

In order to throw light on the cause of these internal strains, we will further analyze the load-depth dependences $P(h)$ of the Si substrate and of ZnSnO/Si CSs with different film thickness (Fig. 8).

It is known [27–32], that a mixed-type amorphous-crystalline structure is formed in the material volume in the region of the imprint for single crystalline Si starting from the applied load of $P_{max} \approx 30$ mN. This modification of the crystal structure is evidenced on the $P(h)$ curve by the "elbow" effect (Fig. 8a, curve 1). A Si-III phase with cubic structure with VS8 centered faces and/or a Si-XII phase with *rhombohedral* R8 structure are generated with increasing the magnitude of the load. These structures are evidenced by the "pop-out" effect in the $P(h)$ diagram (Fig. 8c, curve 1). Both the "pop-out" and the "elbow" effects are observed in the respective diagrams in the case when both the mentioned phases are present. (Fig. 8b, curve 1). Taking into account the regularities inherent to the indentation of Si, we

will compare the $P(h)$ curves in Fig. 8, in order to assess the deformation process evolution of ZnSnO/Si structures with different thickness of the films, and the substrate contribution to mechanical parameters modification as a function of the magnitude of the applied load, and, respectively, of the imprint depth h.
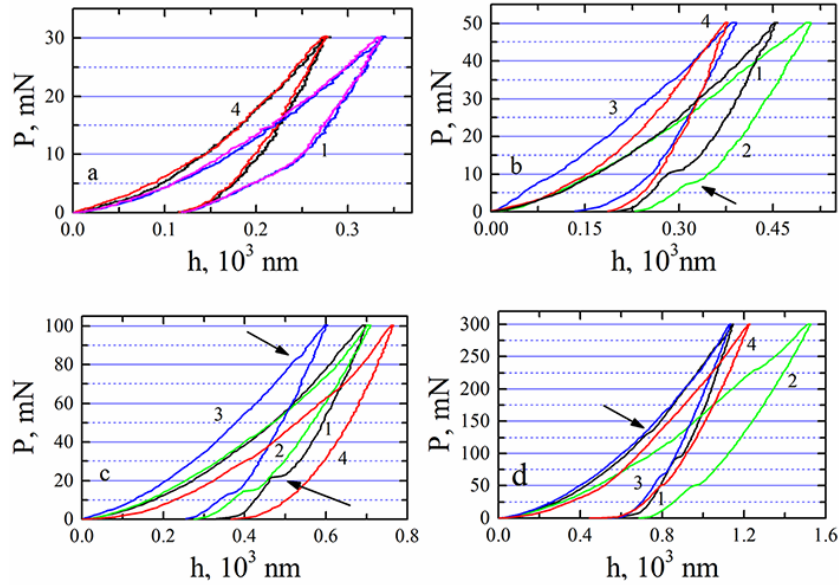

Fig. 8 – "Load-depth" $P(h)$ dependencies of ZnSnO/Si CSs at different values of the P_{max} applied load as follows: (a) is for 30 mN, (b) is for 50 mN, (c) is for 100 mN, (d) is for 300 mN. Curves 1 belong to the Si samples. Curves 2, 3, 4 are for ZnSnO/Si samples with t_1, t_2, t_3 film thickness, respectively. Arrows indicate "pop-in", "elbow" and "pop-out" effects.

Both the form and the order of $P(h)$ curves location depending on the film thickness and the increase of the indenter depth penetration present interest in the case of our investigations.

The curves for the Si substrate and for the ZnSnO/Si structure with the thickest film ($t_3 = 1410$ nm), subjected to deformation up to a load of $P_{max} = 30$ mN, are presented in Fig. 8a. The "elbow" effect is observed on the Si curve at the unloading stage, while the curve for the ZnSnO/Si structure does not exhibit specific characteristics, and it evolves quite uniformly during the entire loading-unloading process. This fact serves as a demonstration that the whole plastic deformation is concentrated in the film volume, while the Si substrate does not participate in the penetration process of the ZnSnO/Si structure with the third ($t_3 = 1410$ nm) film.

For the magnitude of the load of $P_{max} = 50$ mN (Fig. 8b), the $P(h)$ curves corresponding to the loading stage demonstrates a quite smooth deformation for all the samples. For the curves corresponding to the unloading stage, one can see that the "pop-out" + "elbow" effect is present only on curves corresponding to the

deformation of the Si crystal substrate and of the ZnSnO/Si structure with the thinner film of $t_1 = 445$ nm. Only the "elbow" effect is observed on the curve 3, which may serve as a demonstration that the influence of the crystal substrate is reduced in the process of penetration for the thicker film $t_2 = 670$ nm as compared to the film with $t_1 = 445$ nm. The influence of the substrate is even weaker in the deformation of the structure with the film of $t_3 = 1410$ nm, as indicated by the curve 4 in Fig. 8b, which is practically similar to the curve 4 in Fig. 8a, except for a small difference at the end of the unloading curve, its form resembling the "elbow" effect. It means that decreasing of the substrate contribution occurs with increasing the film thickness for this load during the nanoindentation of the film/substrate structures. A very weak contribution of the substrate can be deduced for the sample 4 (film thickness of $t_3 = 1410$ nm) when the load changes from 30 mN to 50 mN.

The effect becomes even more pronounced for the next two loads of $P_{max} = 100$ mN şi 300 mN (Fig. 8 c, d). The "pop-out" and "elbow" effects are observed on the unloading curves for ZnSnO/Si samples with $t = 445$ nm and 670 nm. In the case of the film with thickness of $t_3 = 1410$ nm, only the "elbow" effect is revealed in the unloading curve at $P_{max} = 100$ mN, while a weak "pop-out" effect is observed at $P_{max} = 300$ mN (Fig. 8d).

Therefore, one can suggest that the film thickness (t) and the value of the applied load P are factors, which have an opposite influence upon the substrate contribution in the penetration process. The increase of the load P leads to the increase of the Si substrate contribution, while the increase of the film thickness t leads to the weakening of this effect.

Additional important information can be extracted from the comparison of light microscopy images with the $P(h)$ curves, as well as from the analysis of AFM images and the profiles. As mentioned above, the $P(h)$ curves at the loading stage demonstrate a smooth path, but with some weakly pronounced "pop-in" effects, which may come from structural modifications, or from emerging of some cracks either in the Si substrate, or on ZnSnO/Si structures (Fig. 8 c, d) [29, 30, 32]. However, if one compares the number of "pop-in" effects with the data from the image shown in Fig. 6, one can find that the number of cracks around the imprints is much bigger than the number of "pop-in" effects. This observation demonstrates that the cracks around the imprints, as well as the respective relief created at the stage of indenter extraction from the material bear a relaxation character.

The results of investigations with AFM microscopy represent an additional argument in favor of these assumptions (Figs. 9, 10). Figure 9 shows the 3D images of imprints and their profiles formed on the Si single crystal substrate by two loads of 50 mN and 100 mN. One can see that the imprints are plastic for both the loads, without cracks and damages, material pile-ups being formed at their sides. The formation of these pile-ups is a consequence of the plastic displacement of the material upon the indenter removal, as a result of relaxation of the internal energy, which is accumulated in the volume under the imprint. The internal energy is determined by the value of the maximum load and, as a consequence, by the

creation a characteristic hydrostatic compression region under the imprint at the applied load. This effect is accompanied by a phase transition of the Si from the usual Si-I to its Si-II phase. Phase transitions to new structures of Si-III, Si-XII and a-Si phases occur upon unloading, which lead to the volume increase and the displacement of material to the surface in the form of pile-ups [32–34].
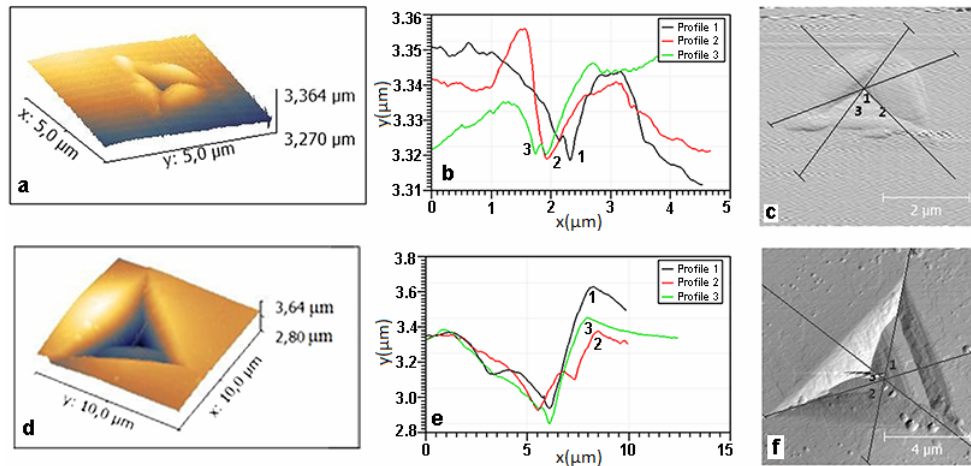

Fig. 9 – AFM imprints produced on the Si (111) single crystal substrate with two P_{max} loads as follows: a, b, c are for 50 mN; d, e, f are for 100 mN. (a, d) are 3D imprint images; (b, e) are profiles of the imprints; (c, f) are 2D images with indication of sections for the profiles.

The size of the pile-ups increases with increasing the value of the load and, respectively, with increasing the area and the depth of imprint, as one can see from Fig. 9. The creation of pile-ups around the imprints on Si puts pressure on the film from below, and the higher is the contribution of the Si substrate in the formation of the complex imprint on the ZnSnO/Si film-substrate structure the stronger is the pressure. Therefore, the analysis of the microstructure and the size of pile-ups on the ZnSnO/Si structure provide information about the degree of the contribution of the substrate to the film deformation.

The evolution of the microrelief changing and the pile-ups size for structures with different thickness of films (t_1, t_2, t_3) as a function of the load value (P_{max}) is presented in Fig. 10. The result for the ZnSnO/Si structure with the t_1 film thickness of 445 nm is shown in Fig. 10 a-f for two loads of P_{max} = 50 and 100 mN. Pile-up effects are clearly observed around the imprints in both the cases. As expected, the magnitude of the pile-up for the load of 100 mN is higher as compared to that of 50 mN. On the other hand, the pile-up effect practically disappears for the film with t_2 = 670 nm thickness at the load of P_{max}=50 mN (compare Fig. 10 a, b, c with Fig. 10 g, h, i). It is clearly observed from Fig. 10 h that the surface relief around the imprint is comparable to the roughness of the sample itself.
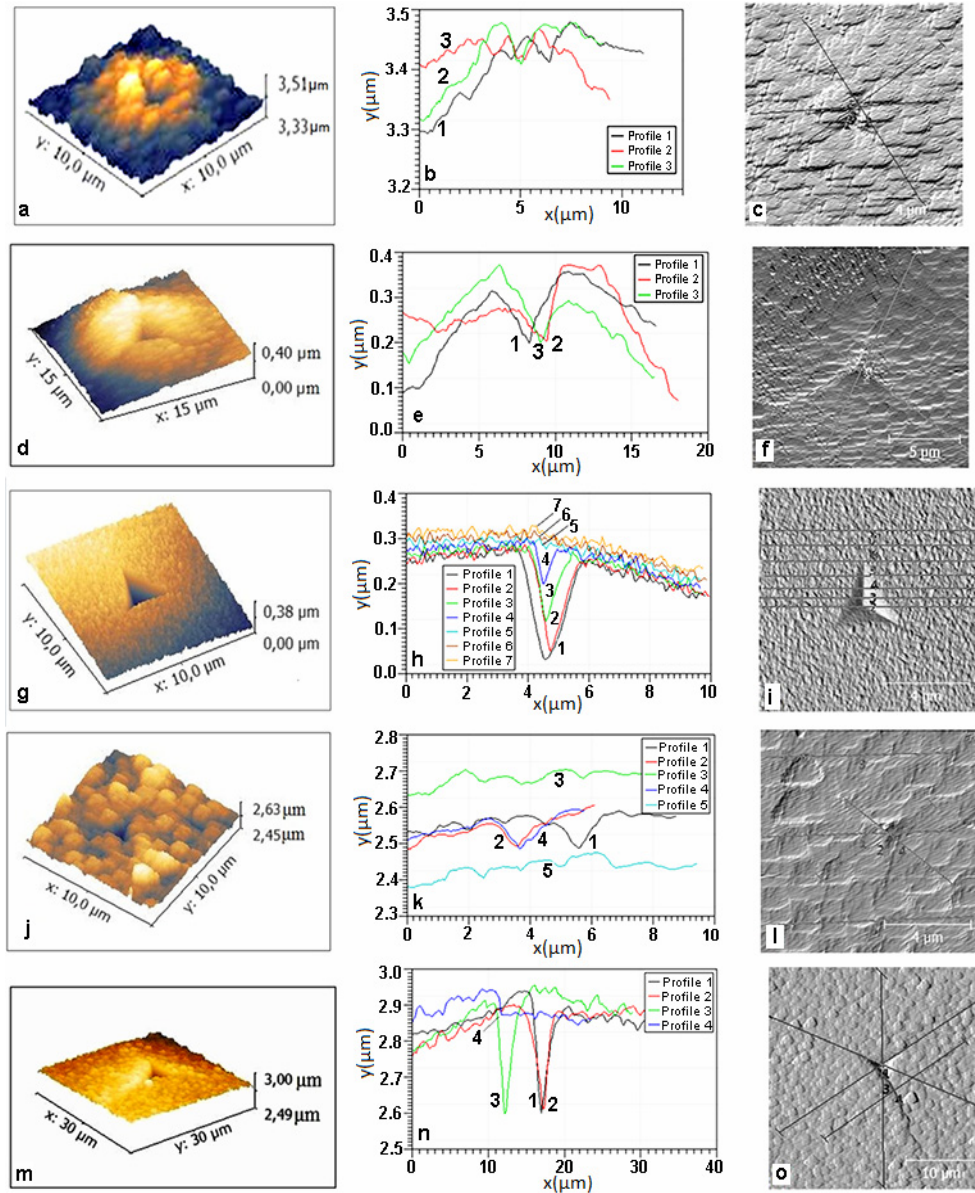
Fig. 10 – AFM imprints produced on ZnSnO/Si CSs with film thickness of $t_1 = 445$ nm (a-f), $t_2 = 670$ nm (g-i), $t_3 = 1410$ nm (j-o), with different P_{max} loads as follows: (a-c, g-i, j-l) are for 50 mN; (d-f, m-o) are for 100 mN. (a, d, g, j, m) are 3D imprint images; (b, e, h, k, n) are profiles of the imprints; (c, f, i, l, o) are 2D with indication of sections for the profiles. Curves 1–4 in (h) represent imprint profile as it moves away from the center to the imprint tip, while curves 5–7 are profiles of the sample surface outside the imprint. Curves 1, 2, 4 in (k) are imprint profiles, while curves 3, 5 are profile of the sample surface outside the imprint. Curves 1, 2, 3 in (n) are imprint profiles, while curve 4 represents the relief of the crack intersection.

This observation reveals the effect of the film thickness, indicating that the contribution of the substrate in the formation of the imprint for the same load decreases with increasing the film thickness, which corroborates the literature data [35]. This effect was confirmed also for the sample with film thickness of $t_3 = 1410$ at $P_{max} = 100$ mN. Since the film thickness increased, the pile-ups were absent around the imprint at $P_{max} = 50$ mN (Fig. 10 j, k, l), and they were hardly observed for the imprint at $P_{max} = 100$ mN (Fig. 10 j, k, l). One can see also that a small crack appeared at a corner of the imprint (see Fig. 10, profile 4).

Therefore, the performed investigations revealed the contribution of two factors (the film thickness t, and the value of the load applied to the indenter), which influence on the nanomechanical properties of film-substrate structures, such as the Young modulus, hardness, strength, plasticity and fragility. The contribution of these factors is manifested in changing the size of the produced imprint.

The results of measuring the depth of the imprint for various combinations of t and P_{max} are presented in Table 3. One can see that the imprint depth (h_{max}) increases naturally with increasing the load. It is 220 nm for $P_{max} = 30$ mN and it varies in the interval of $h_i = 310$–375 nm for $P_{max} = 50$ mN, while for the $P_{max} = 300$ mN it exceeds the thickness of the films t_1 and t_2 and it approaches the film thickness t_3.

Table 3

Values of absolute (h_{max}) and relative (β) imprint depths at different values of t and P_{max} for the ZnSnO/Si CSs. H is the composite hardness of the film-substrate structure

P_{max}, mN	h_{max}, nm			$\beta = h_{max}/t_i$		
	1	2	3	4	5	6
	$t_1 = 445$ nm	$t_2 = 670$ nm	$t_3 = 1410$ nm	$t_1 = 445$ nm	$t_2 = 670$ nm	$t_3 = 1410$ nm
30	–	–	220	–	–	0.16 (H=17 GPa)
50	375	330	310	0.94 (H=11 GPa)	0.47 (H=14 GPa)	0.22 (H=15.7 GPa)
100	530	500	500	1.32 (H=11.5 GPa)	0.71 (H=13 GPa)	0.36 (H=13.3 GPa)
300	1130	1300	1240	2.82 (H=8.6 GPa)	1.86 (H=6.6 GPa)	0.88 (H=7.9 GPa)

Therefore, the deformation created with the same load in films with thickness t_1, t_2, t_3 undergoes different contributions from the substrate. It means that the maximum depth of the imprint cannot serve as a parameter which is responsible for the strength properties of film-substrate structures.

As shown in previous studies [36–39], the relative depth of the imprint, *i.e.* the depth normalized to film thickness ($\beta = h_{max}/t_i$) is a parameter characterizing the nanomechanical properties of film-substrate structures. The integral response of

film and substrate to nanometer scale indentations is characterized by the composite hardness. A relation was established between the composite hardness (H) of a film-substrate structure and the β parameter. Three important regions were identified on the $H(\beta)$ curves, namely, **I** with $\beta \approx 0.1$; **II** with $\beta \approx 1$, and **III** with $1 < \beta < 10$. If the value of β is about 0.1, then the composite hardness approaches the real hardness of the film. The hardness undergoes mutual influence of the film and the substrate when β values is close to unity, while the hardness is mainly determined by properties of the substrate when $\beta > 1$.

Similar three regions can be found in the investigated ZnSnO/Si CSs (Table 3, columns 4–6), but with boundaries of the three regions slightly shifted to lower β values. Namely, the first region with $\beta = 0.16$ corresponds to the real nanohardness of the ZnSnO film equal to 17 GPa. The second region with $0.2 < \beta < 0.5$ is a region of mutual influence of the film and substrate. In this region, $H = 15.7$ GPa for $\beta = 0.22$, $H = 13.3$ GPa for $\beta = 0.36$, and $H = 14$ GPa for $\beta = 0.47$. The third region with $\beta > 0.5$ is a region of the dominant influence of the substrate. Such a region is realized for different combinations of films thicknesses and loads as follows: for the film with thickness t_1, at all the value of the load; for the film with thickness t_2, at the values of the load of $P_{max} = 100$ and 300 mN; for the film with thickness t_3, at the value of the load of $P_{max} = 300$ mN only.

Therefore, investigations of ZnSnO/Si coated systems corroborate the regularities previously discovered for other structures of the film-substrate type. Taking into account that the real nanohardness of the ZnSnO film at a load of 30 mN equals 17 GPa, while the hardness of the Si single crystal substrate is 12.3 GPa at the same load, one can conclude that the investigated ZnSnO/Si structure belongs to coating systems of the "hard-on-hard" type, exhibiting nanomechanical parameters inherent in such materials.

5. CONCLUSIONS

The results of this study demonstrate that the ZnSnO films with submicron thickness (around 400 nm), composed of SnO_2 crystalline microplates (300 nm – 1 μm) and a small amount of Zn_2SnO_4 nanocrystals with the mean size around 20 nm dispersed between SnO_2 micro-crystallites, exhibit better nanomechanical properties as compared to pure SnO_2 crystalline films with similar thickness and roughness. The value of the plasticity index of such a composite film, defined as the ratio between the hardness and the Young modulus (H/E), which describes the wear resistance of the material, is much higher than its value for the Si substrate, or its value for the pure SnO_2 film deposited on the Si substrate, for all the applied loads. The value of this parameter for the composite film increases by around 50% with increasing the load from 50 mN to 300 mN, while its value decreases with increasing the load for the pure SnO_2 film.

Two factors were found to contribute to the nanomechanical properties of film-substrate structures, namely, the film thickness and the value of the load applied to the indenter. These two factors have opposite effects upon the contribution of the substrate to the indentation process. The increase of the load leads to increasing the substrate contribution, while the increase of the film thickness results to decreasing the substrate contribution. A relation was established between the composite hardness of a film-substrate structure and the $\beta = h_{\max}/t_i$ parameter, *i.e.* the relative depth of the imprint. Three important regions were found for ZnSnO films deposited on Si substrates, namely, the first region with $\beta = 0.16$, corresponding to the real nanohardness of the ZnSnO film; the second region with $0.2 < \beta < 0.5$, corresponding to the mutual influence of the film and substrate; and the third region with $\beta > 0.5$, in which there is a predominant influence of the substrate.

It was demonstrated that the ZnSnO films have a high nanohardness of around 17 GPa. Since the hardness of the Si substrate is 12.3 GPa, one can conclude that the investigated ZnSnO/Si structure belongs to coating systems of "hard-on-hard" type, exhibiting plastic and strength properties characteristic for this class of coated systems.

REFERENCES

1. S. R. V. Siva Prasanna, K. Balaji, S. Pandey, S. Rana, Chapter 4 in *Nanomaterials and Polymer Nanocomposites: Raw Materials to Applications*, Ed. N. Karak, Elsevier Inc., Amsterdam, 2019, pp. 123–144.
2. S. A. Corr, in *Nanoscience: Nanostructures through Chemistry*, Vol. 1, P. O'Brien ed., RSC publishing, 2013, pp. 180–207.
3. U. Ozgur, Y.I. Aliliv, C. Liu, A. Teke, M.A. Reshchikov, S. Dogan, V. Avrutin, S.-J. Cho, M. Morkoc, J. Appl. Phys. **98**, 041301 (2005).
4. C. Jagadish, S. Pearton (eds), *Zinc Oxide Bulk, Thin Films and Nanostructures, Processing, Properties and Applications*, Elsevier Science, Amsterdam, 2006.
5. V. S. Bhati, M. Hojamberdiev, and M. Kumar, Enhanced sensing performance of ZnO nanostructures-based gas sensors: A review, Energy Reports. **Suppl. 4**, 46–62 (2020).
6. M. Batzill, U. Diebold, Prog. Surf. Sci. **79**, 147–154, (2005).
7. S. Das, V. Jayaraman, Prog. Mater. Sci. **66**, 112–255 (2014).
8. J. S. Chen, X. W. Lou, Small **9**, 1877–1893 (2013).
9. S. Sun and S. Liang, Mater. Chem. A **5**, 20534–20560 (2017).
10. S. S Nalimova, A.I. Maksimov, L. B. Matyushkin, V. A. Moshnikov, Glass Phys. Chem. **45**, 251–260 (2019).
11. S. J. Mohammed, K. A. Aadim, M. A. Ameen, Kirkuk Univ. J. Sci. Stud. **13(4)**, 96–112 (2018).

12. M. N. Mullings, C. Hägglund, J. T. Tanskanen, Y. Yee, S. Geyer, S. F. Bent, Thin Solid Films, **556**, 186–194 (2014).
13. Y. Zhao, L. Hu, H. Liu, M. Liao, X. Fang, L. Wu, Sci. Reports **4**, 6847 (2014).
14. D.-L. Young, D. L. Williamson, T. J. Coutts, Structural characterization of zinc stannate thin films, J. Appl. Phys. **91**, 1464–1471 (2002).
15. H. Jung, Y. Park, S. Gedi, V. Reddy, M. Reddy, G. Ferblantier, W. K. Kim, Korean J. Chem. Eng. **37**, 730–735 (2020).
16. I. Saafi, R. Dridi, A. Mhamdi, Optik. **126**, 4382–4386 (2015).
17. M. A. Patil, S. Mujawar, V. V. Ganbalve, H. Deshmukh, J. Mater. Sci.-Mater. El. **27**, 12323–12328 (2016).
18. R. Dridi, I. Saafi, A. Mhamdi, A. Matri, A.Yumak, M. Haj Lakhdar, A. Amlouk, K. Boubaker, J. Alloy. Comp. **634**, 179–186 (2015).
19. W. C. Oliver, G. M. Pharr, J. Mater. Res. **7**, 1564–1583 (1992).
20. W. C. Oliver, G. M. Pharr, J. Mater. Res. **19**, 3–20 (2004).
21. J. E. Jeronsia, A. Joseph, M. M. Jaculine, S. J. Das, J. Taibah Univ. Sci. **10**, 601–606 (2016).
22. S. Dinesh, S. Barathan, V. K. Premkumar, G. Sivakumar, and N. Anandan, J. Mater Sci: Mater Electron **27**, 9668–9675 (2016).
23. A. Patterson, Phys. Rev. **56**, 978–982 (1939).
24. D. Grabco, E. Harea, O. Shikimaka and D. Sherban, in: *Horizons in World Physics*, Ed. A. Reiner, Nova Publisher, Inc. **277**, 111–130, 2012.
25. A. Leyland, A. Matthews, Wear **246**, 1–11 (2000).
26. J. Musil, Surf. Coat. Tech. 2000 **125**, 322–330 (2000).
27. D. Grabco, E. Harea, Surf. Eng. Appl. Electrochem. **49**, 36–41 (2013).
28. A. P. Gerk, D. Tabor, Nature **271**, 732–733 (1978).
29. G. M. Pharr, W. C. Oliver, D. R. Clarke, J. Electr. Mater. **19**, 881–887 (1990).
30. V. Domnich, Y. Gogotsi, Rev. Adv. Mater. Sci. **3**, 31–36 (2002).
31. T. Juliano, Y. Gogotsi, V. Domnich, J. Mater. Res. **18**, 1192–1201 (2003).
32. I. Zarudi, J. Zou, C. Zhang, Appl. Phys. Let. **82**, 874–876 (2003).
33. D. Stone, W. R. LaFontaine, P. Alexopoulos, W. Wu, L. Che-Yu, J. Mater. Res. **3**, 141–147 (1988).
34. S. Ruffell, J. E. Bradby, N. Fujisawa, J. S. Williams, J. Appl. Phys. **101**, 083531 (2007).
35. S. Suresh, T.-G. Nieh, B. W. Choi, Scripta Materialia **41**, 951–957 (1999).
36. A. M. Korsunsky, M. R. McGurk, S. J. Bull, T. F. Page, Surf. Coat. Technol. **99**, 171–183 (1998).
37. J. Tuck, A. M. Korsunsky, D. G. Bhat, S. J. Bull, Surf. Coat. Technol. **139**, 63–74 (2001).
38. A. Shuguro *et al.*, J. Korean Powder Metallurgy Inst. **10**, 190–194 (2003).
39. R. Saha, W. D. Nix, Acta Materialia **50**, 23–38 (2002).